HR Diagram of M20 and M7

June 12, 2023

1 Introduction

The Hertzsprung-Russell (HR) diagram serves as a fundamental tool in astrophysical research, facilitating the exploration of stellar evolution dynamics. This diagram, which delineates the relationship between stellar luminosities and temperatures, provides a comprehensive representation of various stages in stellar life cycles.

The focus of this study is on the observations of two distinct astronomical entities, M20 (the Trifid Nebula) and M7 (the Ptolemy C luster). M20, a star-forming region, presents a unique opportunity to scrutinize the initial stages of stellar formation. Conversely, M7, an open cluster abundant with bright stars, enables the observation of stars that are in more advanced stages of their evolutionary trajectory. The objective of plotting these stars on the HR diagram is to elucidate the progression and influencing f actors o f stellar evolution.

The current research landscape in the study of the Hertzsprung-Russell (HR) diagram and stellar evolution is characterized by a multifaceted approach that combines various observational techniques and theoretical models. For instance, Monteiro's work on "Asteroseismology across the HR diagram" [6]underscores the importance of integrating asteroseismology with high precision spectroscopy to gain a nuanced understanding of stellar structure and evolution across the HR diagram. This is complemented by the study by Ramirez et al., "Granulation across the HR diagram," [9] which emphasizes the need for ultra-high quality spectra and the application of stellar surface convection models to interpret stellar properties accurately. Meanwhile, Humphreys' "The Complex Upper HR Diagram" [4] highlights the complexities inherent in interpreting HR diagrams, particularly for the most luminous stars, underscoring the importance of meticulous analysis. Adding another layer of complexity, Eyer and Mowlavi's "Variable stars across the observational HR diagram" [3] discusses the distribution and significance of variable stars in understanding stellar structure and evolution. Lastly, Kurtz's "Asteroseismology and the HR diagram" [5] reiterates the pivotal role of asteroseismology in studying stars across the HR diagram. Collectively, these studies provide a comprehensive backdrop for the current project, which leverages photometry and color indices to study stars in M7 and M20, contributing to the broader understanding of stellar evolution.

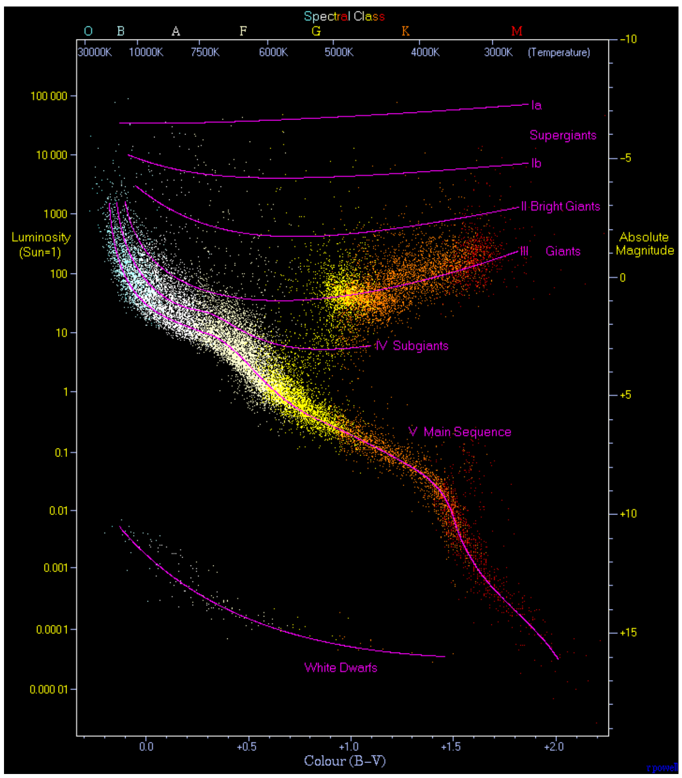

Figure 1: An illustrative Hertzsprung-Russell (HR) diagram sourced from Wikipedia. The diagram presents a color-coded scatter plot with the B-V color index on the x-axis and the B magnitude on the y-axis. The B-V color index serves as a proxy for the effective temperature of stars, allowing for the categorization of stars into different stages of their life cycles. This classic representation of the HR diagram provides a comprehensive overview of stellar evolution. [10]

The observations were conducted using the Las Cumbres Observatory

(LCO), leveraging its capabilities for remote and automated observations. The observation window for M20 and M7 was ascertained using the calculator on the LCO website. Subsequently, images obtained in the B and V bands were processed using the astropy.io package for photometry, and the HR diagram was generated employing the color index method.

The significance of this research transcends academic interest. Comprehending stellar evolution is integral to understanding the universe. Stars, as the building blocks of galaxies, play a crucial role in the distribution of elements throughout the universe. Furthermore, the study of stars and their evolution is inherently linked to the search for exoplanets and the pursuit of extraterrestrial life. Refining our understanding of stars enhances our capability to identify potential life-harboring planets.

While this research may appear to traverse well-trodden paths, it is the continuous refinement and revalidation of our understanding of such fundamental topics that fortify the foundation of astrophysics. The incorporation of modern techniques and technologies in this study contributes to this ongoing process.

Future research directions include delving deeper into specific aspects of stellar evolution. The data from M20 could be further analyzed to understand the intricacies of stellar formation, while the bright stars of M7 could be studied to explore later stages of stellar life cycles. The quest to understand the stars is far from complete, and each step forward brings us closer to deciphering the mysteries of the universe.

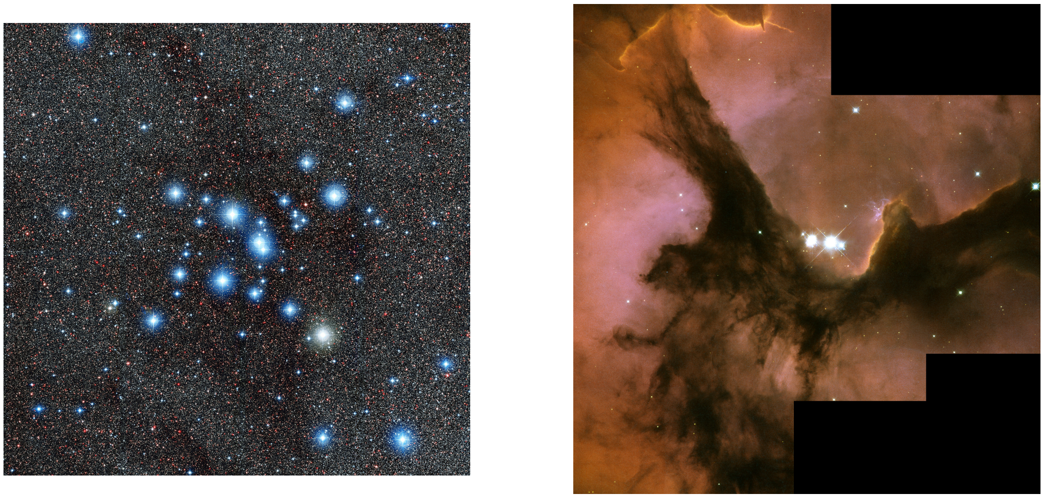

Figure 2: Color composite images of M20 (the Trifid Nebula, right) [7] and M7 (the Ptolemy Cluster, left) [11]. M20, a vibrant star-forming region, and M7, an open cluster abundant with bright stars, represent different stages of stellar evolution. The images, captured through multiple filters, reveal the diverse stellar population within these astronomical entities. The varying colors of the stars, indicative of their different temperatures, offer a rich field for the study of stellar life cycles. These images form the basis for their representation on the Hertzsprung-Russell (HR) diagram, enhancing our understanding of stellar evolution

2 Methods

The methodology employed in this study encompasses both theoretical and observational approaches, with the aim of ensuring the reproducibility of the results.

2.1 Theoretical Methods

The theoretical foundation of this study is based on the principles of stellar evolution and the construction of the Hertzsprung-Russell (HR) diagram. The HR diagram is a scatter plot that represents the relationship between the luminosities and temperatures of stars, providing a comprehensive overview of various stages in stellar life cycles.

A key theoretical method employed in this study is the color index method.

This method is based on the principle of black body radiation, which states that stars emit light at different wavelengths and intensities depending on their temperature. By measuring the magnitude of stars in different wavelength bands, we can determine the color of the star, which serves as a proxy for its temperature. Bluer stars, which have a lower color index, are hotter, while redder stars, with a higher color index, are cooler. This method allows us to plot the stars on the HR diagram based on their color indices.

$$B(\lambda, T) = \frac{2hc^2}{\lambda^5} \frac{1}{e^{\frac{hc}{\lambda k T}} - 1} \tag{1}$$

This study also employs the use of Sloan Digital Sky Survey (SDSS) filters to calculate color indices. The central wavelength and full width at half maximum (FWHM) of the SDSS filters were used, assuming a unit response within the range of the central wavelength plus or minus the FWHM/2, and zero response otherwise. The stars were assumed to obey black body radiation, and the flux for each band at a given temperature was calculated through integration. The flux was then used to calculate the magnitude, and the difference in magnitude between each band was used to calculate the color indices. This method provides a more detailed and accurate representation of the color and temperature of the stars, enhancing the precision of the HR diagram. Importantly, the zero point temperature was set to be 10800K in this study, providing a reference point for the calculation of color indices.

$$S(\lambda) = \begin{cases} 1 & \text{if } \lambda_c - \frac{FWHM}{2} \leq \lambda \leq \lambda_c + \frac{FWHM}{2} \\ 0 & \text{otherwise} \end{cases} \tag{2}$$

$$\text{Color Index} = -2.5 \log_{10} \left(\frac{f_1}{f_2} \right) \tag{3}$$

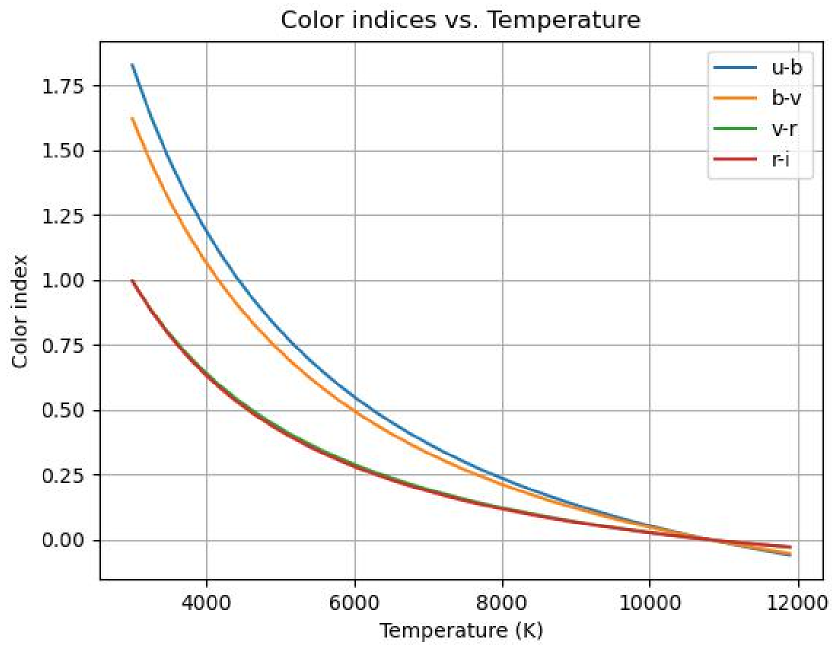

Figure 3: Plot of color indices versus temperature for various bands (u-b, b-v, v-r, and r-i), each represented in a distinct color. The x-axis represents the temperature, while the y-axis represents the color indices. This plot provides a comprehensive view of the relationship between stellar temperature and color indices across different bands. The trend lines illustrate the correlation between increasing temperature and decreasing color index, consistent with the principles of black body radiation. This graphical representation aids in understanding the color-temperature relationship, a fundamental aspect in the construction of the Hertzsprung-Russell (HR) diagram.

The color index versus temperature plot generated in this study adheres to the principles of black body radiation and Wien's displacement law. The color index, a measure of the difference in magnitude between two different wavelength bands, serves as a quantifiable representation of a star's color, which is directly correlated to the star's temperature.

As per Wien's displacement law, the peak wavelength of the radiation emitted by a black body is inversely proportional to its temperature. Consequently, a star with a higher temperature emits more light in the shorter (bluer) wavelength bands, resulting in a lower magnitude in the blue band compared to the red band. This leads to a lower (or more negative) color index. Conversely, a star with a lower temperature emits more light in the longer (redder) wavelength bands, resulting in a higher color index.

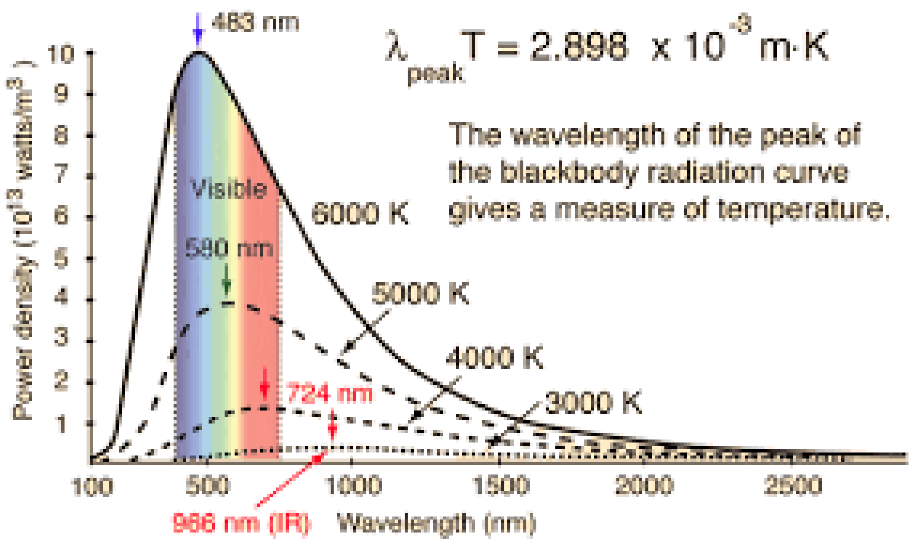

Figure 4: This plot [1] illustrates the spectral intensity of black body radiation as a function of frequency for various temperatures. The curves represent the Planck's law prediction, showing that as the temperature increases, the peak of the black body radiation curve shifts to higher frequencies. This phenomenon is known as Wien's Displacement Law. The area under each curve also increases with temperature, indicating a greater total energy emission, as described by the Stefan-Boltzmann Law.

The observed trend of a decreasing color index with an increasing temperature in the plot aligns with these principles, reinforcing the validity of the color index method employed in this study.

2.2 Observational Method

The observational data for this study were acquired using the 0.4m class telescopes in the Las Cumbres Observatory (LCO) network. The LCO network comprises a global array of robotic telescopes that can be remotely controlled, providing the capability for continuous observations across different time zones. The 0.4m telescope is equipped with an SBIG CCD camera, which is sensitive across the optical wavelength range, making it suitable for capturing images in the B and V bands. The telescope also has a set of standard Johnson-Cousins filters, which were used to obtain the B and V band images required for the color index method.

The observation window for M20 and M7 was determined using the LCO's observation portal [8], which provides a calculator for determining the optimal observation times based on the target's coordinates and the desired date range.

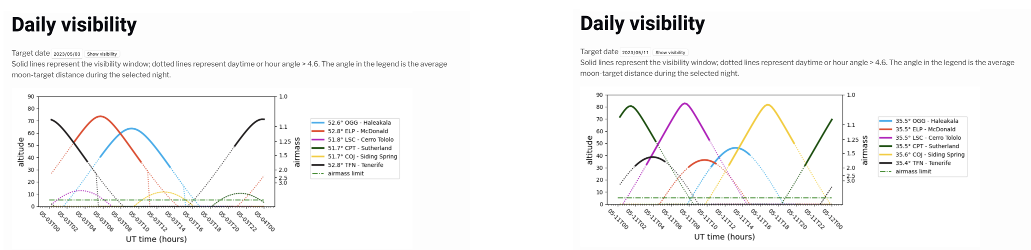

Figure 5: Observation windows for M7 (the Ptolemy Cluster, left) and M20 (the Trifid Nebula, right) calculated using the Las Cumbres Observatory (LCO) tool. The plots depict the optimal time periods for observing these astronomical entities, taking into account factors such as their celestial coordinates and the observer's location. The observation windows are crucial for planning the data acquisition process, ensuring the collection of high-quality images for subsequent analysis and the construction of the Hertzsprung-Russell (HR) diagram.

The raw images obtained from the observations underwent a pre-processing stage to correct for instrumental effects. This included bias subtraction, dark current correction, and flat fielding, which are standard procedures in CCD image processing. In addition, background subtraction was performed to reduce errors from background noise.

The pre-processed images were then used for photometric analysis. The photometric analysis was conducted using the astropy.io package, a Python library for astronomy and astrophysics. This package provides tools for handling astronomical data formats, performing astronomical calculations, and conducting image processing and data analysis.

The specific steps in the photometric analysis included source detection on the images, aperture photometry to measure the brightness of the detected sources, and the calculation of the color index for each source. The color index, obtained by subtracting the V band magnitude from the B band magnitude for each source, was then used to plot the sources on the HR diagram.

2.3 Photometry Procedure

The photometry procedure implemented in this study incorporated several Python packages, including astropy.io, astroalign, and photutils, to facilitate the identification of stellar positions, the measurement of stellar brightness, and the calculation of color indices.

Initially, the visibility of the images was adjusted utilizing the PercentileInterval function in astropy.io, which set the vmin and vmax values to delineate the range of pixel values displayed in the image.

Subsequently, the images in the B and V bands were aligned employing the register function in the astroalign package, ensuring consistent star comparison when calculating the color index.

Background noise in the images was estimated via the mad_std function in *astropy.stats*. This value informed the threshold for star detection in the DAOStarFinder function in the photutils package, with the threshold set to 15 times the background noise to ensure detection of significant sources only.

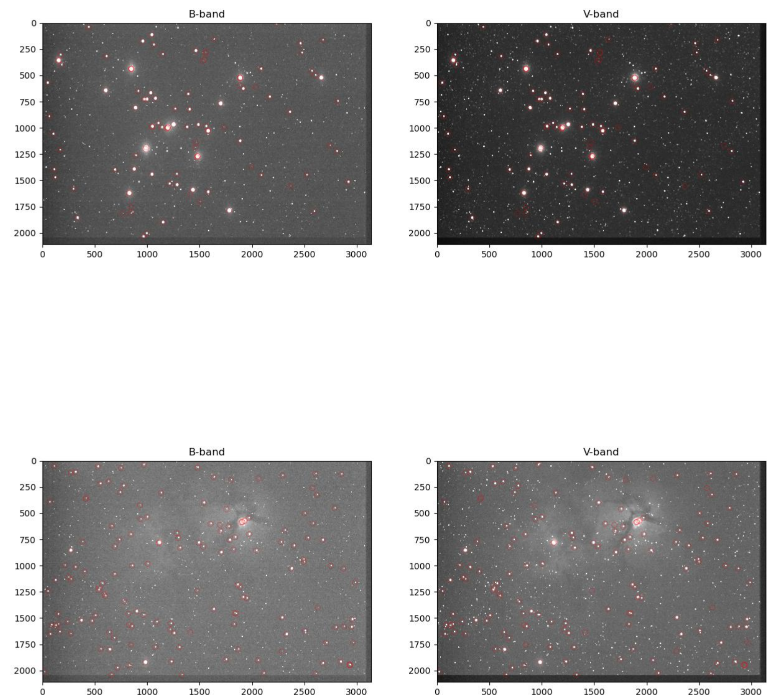

Figure 6: Results of the DAOStarFinder algorithm applied to the B band and V band images of M7 (the Ptolemy Cluster, upper) and M20 (the Trifid Nebula, lower). The plots illustrate the detected stars within these astronomical entities, as identified by the algorithm. The varying densities and distributions of the detected stars reflect the distinct stellar populations within M7 and M20.

Background subtraction was conducted using the MedianBackground and Background2D functions in astropy.io, with a box size of (70, 70) and a filter size of (25, 25). The box size represents the area affected by each star, while the filter size is proportional to the estimated size of the stars, reducing the impact of background noise on the photometric measurements.

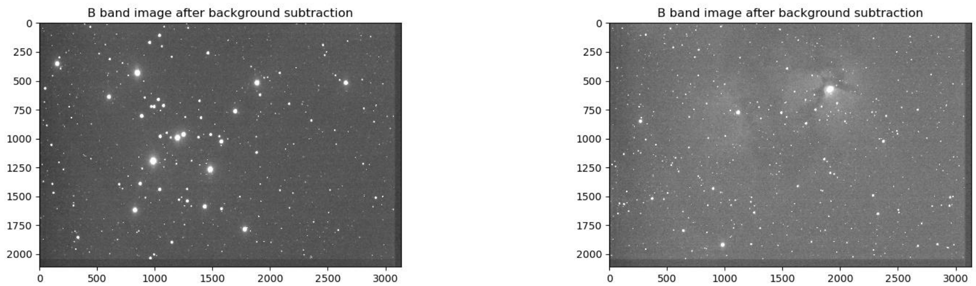

Figure 7: Background subtracted images of M7 (the Ptolemy Cluster, left) and M20 (the Trifid Nebula, right) with a PercentileInterval set to 99. The subtraction of the background noise enhances the visibility of the stars and other celestial features within these astronomical entities. The images reveal the rich stellar population within M7 and M20, each representing different stages of stellar evolution.

Aperture photometry was performed using the aperture_photometry function and the *CircularAperture* class in the *photutils* package, measuring the flux of the detected stars in units of electrons.

A bright, isolated star was selected as a reference star for the conversion of flux measurements to magnitudes. The reference star was selected by sorting all the stars by brightness and then defining a function to check the distance to the closest star for each star. This process ensured the selection of the brightest isolated stars, which are less likely to be false positives from the star finder function. The magnitude of the reference star was measured without blending with other stars. The color index for each star was then calculated by subtracting the V band magnitude from the B band magnitude.

The pixel coordinates of the stars were converted to Right Ascension (RA) and Declination (DEC) using the pixel_to_world function in the World Coordinate System (WCS) of *astropy.io*. The RA and DEC coordinates were then used to search the SIMBAD [2]astronomical database for the magnitudes of the reference star in the B and V bands.

The conversion from flux to magnitude was performed using the equation:

$$m = -2.5log(\frac{f}{f_0}) + m_0 \tag{4}$$

where f is the flux of the star, f_0 is the flux of the reference star, and m_0 is the magnitude of the reference star.

The Python packages used in this procedure, particularly the photutils package, were instrumental in automating the star detection and photometry processes. Given the large number of stars in each image, manual aperture drawing would have been impractical.

3 Results

The results of this study are presented in a structured format, incorporating tables, plots, and figures to facilitate comprehension.

3.1 Data Presentation

The primary data from this study are presented in the form of a Hertzsprung-Russell (HR) diagram, which plots the color indices of the observed stars against their magnitudes. The color indices, calculated by subtracting the V band magnitudes from the B band magnitudes, serve as a proxy for the stars' temperatures, while the magnitudes represent their luminosities.

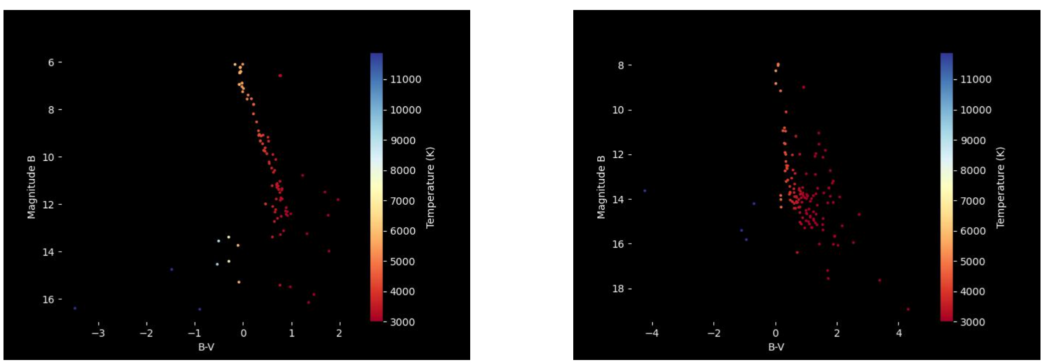

Figure 8: Hertzsprung-Russell (HR) diagrams for M7 (the Ptolemy Cluster, left) and M20 (the Trifid Nebula, right). The diagrams plot the B magnitude (y-axis) against the B-V color index (x-axis) for the stars within these astronomical entities. The color coding represents the effective temperature of the stars, with cooler stars appearing redder and hotter stars appearing bluer. The distribution of stars in these diagrams reflects the distinct stellar populations within M7 and M20, providing insights into their respective stages of stellar evolution

In addition to the HR diagrams, tables of the raw photometric data are also provided. These tables include the pixel coordinates of each star, the B and V band magnitudes, the calculated color index, and the associated errors for each measurement. It should be noted that there are a few empty entries in the photometry tables. These empty entries are indicative of false positives from the DAOStarFinder algorithm, highlighting the inherent challenges in automated star detection and the need for careful data validation.

photometry_table

id	xcenter	ycenter	aperture_sum	magnitude	aperture_sum_error	magnitude_error	color_index	temperature
1	967.0052879919610	38.613057532253700	16794.90144838830	13.593879696031500	414.9338438858970	0.02682413459053730	0.7761018261546580	4800.0
2	113.25751474285900	52.313045171671500	-3251.3317208504600		390.03059063705100	-0.1302451947619410		
3	530.21731542914	55.258636253108100	33226.61185558850	12.853108200006000	434.28309339545600	0.014190940673191000	0.6459057802527430	5300.0
4	1480.1824612035100	64.21562555562210	17963.237302352000	13.520861827560600	416.3393215345980	0.025164432626816200	1.3773925799688900	3400.0
5	749.8791136749010	69.15191768757630	4440.856584791340	15.03815647524970	399.76999629578100	0.09773897226062910	0.803929304691092	4700.0
6	316.70040356934700	108.9730101760390	38107.12015498750	12.704308022067500	439.86624502060300	0.01253253212332740	0.5785146278492410	5600.0
7	271.7731670510260	115.32868226156400	122.71363145793900	18.934591324571500	394.33222919892700	3.48894228666849	4.320146023444740	3000.0
8	2605.4552908390600	123.43744523060500	6609.126890740190	14.606463120177900	402.4727571454720	0.06611754488688980	0.8000813273984240	4700.0
9	2851.4138539970800	128.73658256523600	4118.081632628390	15.120085967010800	399.3660914326180	0.10529325620589700	0.8477247752176410	4600.0
10	2289.3526964553800	140.22947668181500	7217.093023214170	14.51091758774570	403.2273383300690	0.06066133809901140	0.9999553030971830	4200.0
11	1635.0105895740900	158.5778359571710	9558.999918831190	14.205792200652700	406.12090967145300	0.046128274807383600	-0.689848361782671	11900.0
12	2063.1017673047500	169.28018451189600	348.8606431600560	17.800193402645100	394.6188718202640	1.2281465525461800		
13	1799.5212939712700	184.1831987526280	6850.789348106650	14.567471810961500	402.7728673851360	0.06383280264414270		
14	630.5928908546040	198.10921557985000	6187.082003051820	14.678108665051100	401.94810032713100	0.07053561028343530	1.328057793769880	3500.0
15	553.4160307293250	218.44785142163600	24228.916451847500	13.195988364533700	423.79725082329800	0.01899102750262410	1.88587439511414	3000.0
16	774.1557070241640	239.52095787001600	23812.15547896600	13.214826571527700	423.3052667195430	0.019300976517988100	0.35592614591977200	6800.0
17	2574.8201611808000	260.1161754941770	-203.15566786845000		393.9188211873980	-2.1052424005012000		
18	741.7068341570310	302.3215898231660	12203.329805732700	13.940627473898200	409.36355866060000	0.03642127547332610	0.9573998728077020	4300.0
19	1132.669113735630	306.04478832453700	8338.216502094300	14.354140426928900	404.61513794670600	0.052685763694382800	0.8072795072470280	4700.0
20	2617.423077094220	324.7887398606550	2477.7097928398700	15.671697252123100	397.3070640529530	0.17410056056404600	1.925137846419340	3000.0

Figure 9: An excerpt from the photometry table generated from the observations of M7. The table includes the following columns: 'id' for the identification number of the star, 'xcenter' and 'ycenter' for the pixel coordinates of the star in the image, 'aperture_sum' for the total flux within the photometric aperture, 'magnitude' for the calculated stellar magnitude, 'aperture_sum_error' for the estimated error in the total flux, 'magnitude_error' for the propagated error in the stellar magnitude, 'color_index' for the B-V color index, and 'effective temperature' for the estimated effective temperature of the star derived from the color index.

3.2 Error Analysis

The error analysis in this study involves both statistical and systematic considerations. The statistical errors are derived from the Poisson statistics of the photon counts. The Poisson distribution is a discrete probability distribution that expresses the probability of a given number of events occurring in a fixed interval of time or space. In the context of this study, the events are the detection of photons by the telescope. The probability mass function of a Poisson distribution is given by:

$$P(N;\lambda) = \frac{e^{-\lambda}\lambda^N}{N!} \tag{5}$$

Where N is the number of events (in this case, the number of photons detected),λ is the average rate of value (mean number of photons detected). The standard deviation of a Poisson distribution is the square root of the mean, which in this case is the number of photons detected, represented by N. Therefore, the statistical error within the aperture, σ_N,is given by $\sqrt{N}$.

$$\sigma_N = \sqrt{N + n \times \sigma_{\text{bg}}^2} \tag{6}$$

In this equation, N is the aperture sum in unit of electrons, n is number of pixels in the aperture, and σ_{bg} is the standard deviation of the background noise. And error in magnitude is calculated using:

$$\sigma_m = 2.5\frac{\sigma_N}{N\ln(10)} \tag{7}$$

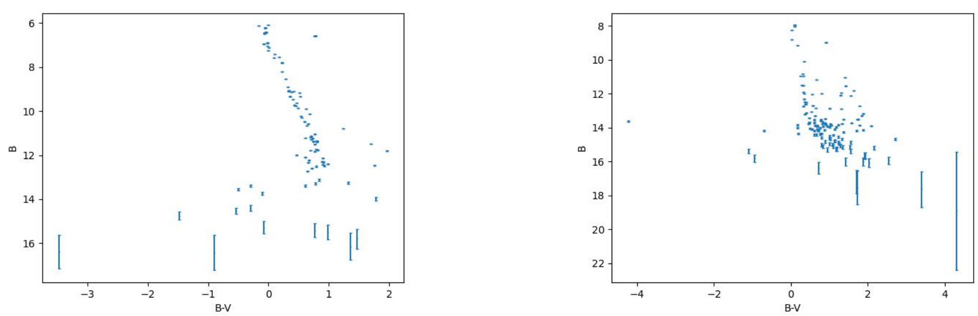

Figure 10: Hertzsprung-Russell (HR) diagrams for M7 (the Ptolemy Cluster, left) and M20 (the Trifid Nebula, right) with error bars. The diagrams plot the B magnitude (y-axis) against the B-V color index (x-axis) for the stars within these astronomical entities. The error bars represent the uncertainties in the B magnitude and B-V color index measurements, reflecting the inherent uncertainties in photometry and color index calculation.

Instrumental errors in this study could arise from several sources, primarily linked to the assumptions made during the observational and data analysis processes. The use of the Las Cumbres Observatory (LCO) telescope, while providing high-resolution images, may also introduce uncertainties due to instrumental limitations. For instance, the telescope's sensitivity across different wavelengths, alignment of the optical components, and the precision of the tracking system could all contribute to the overall instrumental error.

The choice of filters, specifically the Sloan Digital Sky Survey (SDSS) and Bessel filters, also plays a significant role in determining the accuracy of the photometric measurements. The transmission characteristics of these filters, their alignment, and their calibration could introduce systematic errors into the measurements.

The method of propagating color indices in this study is based on the assumption that all stars obey the laws of black body radiation. This assumption allows for the calculation of the flux in each band at a given temperature, which is then used to calculate the magnitudes and color indices. However, real stars do not strictly adhere to the laws of black body radiation due to various factors such as stellar atmospheres and spectral lines, which could introduce systematic errors into the color index calculations.

Additionally, the transmission function, $s(\lambda)$, for the SDSS and Bessel filters was approximated as a box function, with a value of 1 within the central wavelength $\pm$ FWHM/2 region and 0 outside. This approximation simplifies the calculations but may not accurately represent the actual transmission characteristics of the filters, potentially leading to further systematic errors in the photometric measurements.

Furthermore, during the photometry process, it was assumed that all the light within the aperture comes from a single star. This assumption could lead to overestimation of the star's brightness if there are other faint stars within the aperture or if the star's light is scattered due to atmospheric or instrumental effects. This could, in turn, affect the calculated magnitudes and color indices, introducing further uncertainties into the construction of the HR diagram.

Overall, while every effort was made to minimize these errors and uncertainties, their potential impact on the results of this study should be acknowledged. Future improvements could include refining the photometry process, using more precise filters, and incorporating more sophisticated models for stellar radiation into the color index calculations.

3.3 Data Interpretation

The data obtained from this study provide insights into the stellar populations of M20 and M7 under the current astrophysical framework. The HR diagram reveals the distribution of stars in different stages of their life cycles, with hotter, more luminous stars located towards the top left of the diagram and cooler, less luminous stars towards the bottom right.

The data from M20, a star-forming region, show a significant population of hot, luminous stars, indicative of ongoing star formation. Conversely, the data from M7, an open cluster, show a broader distribution of stars, suggesting a more mature stellar population.

The HR diagram generated from the data exhibits the expected shape, with data points extending from the bottom right to the top left. This pattern is consistent with the theoretical HR diagram, providing validation for the observational and data analysis methods used in this study.

Specifically, the HR diagram for M7 shows a clear linear relationship between the B magnitude and the B-V color index, which is consistent with the expected distribution of stars in an HR diagram. This suggests that the stars in M7 are at a similar distance, supporting the assumption of M7 being a relatively homogeneous open cluster.

In contrast, the HR diagram for M20 does not show as strict a linear relationship, which could indicate a variation in the distances of the stars. This is consistent with M20 being a nebula, where stars are in different stages of formation and may not be at the same distance.

The Spearman rank correlation coefficients for M7 and M20 are 0.433 and 0.468 respectively. Despite the higher coefficient for M20, visual inspection of the Hertzsprung-Russell (HR) diagrams suggests a stronger linear relationship for M7. This discrepancy can be attributed to the presence of outliers in the data. The Spearman rank correlation coefficient is a non-parametric measure of correlation, meaning it captures the monotonic relationship between variables, not necessarily linear. It is also less sensitive to outliers compared to the Pearson correlation coefficient. However, in this case, the outliers in the M20 data might have influenced the ranks of the data points, leading to a higher Spearman correlation coefficient. This highlights the importance of considering both statistical measures and visual data inspection in data analysis. It also underscores the need for careful data cleaning and outlier detection in astrophysical studies.

Upon removing the outliers with color indices smaller than -1, the Spearman rank correlation coefficients for M7 and M20 were recalculated to be 0.513 and 0.495, respectively. This adjustment in the correlation coefficients aligns more closely with the visual inspection of the Hertzsprung-Russell (HR) diagrams, which suggested a stronger linear relationship for M7. This outcome supports the initial hypothesis that the discrepancy between the visual inspection and the correlation test results was due to the influence of outliers in the data. The adjustment of the correlation coefficients after outlier removal underscores the impact outliers can have on statistical measures of correlation. It also highlights the importance of thorough data cleaning and outlier detection in ensuring the accuracy of statistical analyses in astrophysical studies.

4 Discussion

The research conducted in this study contributes to the broader understanding of stellar evolution, as represented in the Hertzsprung-Russell (HR) diagram. By observing and analyzing the stellar populations of M20 and M7, this study provides insights into different stages of stellar life cycles, from the early stages of star formation in M20 to the more mature stellar population in M7.

One of the key implications of this research is the potential difference in the stages of stellar evolution in clusters and nebulae. The HR diagram for M7, an open cluster, shows a clear linear relationship between the B magnitude and the B-V color index, suggesting a relatively homogeneous population of stars at similar stages of evolution. In contrast, the HR diagram for M20, a nebula, shows a less strict linear relationship, which could indicate a variation in the distances and thus the stages of formation of the stars. This finding suggests that the assumption of stars in a nebula being at the same distance may not always hold, which has implications for the interpretation of HR diagrams for nebulae and the understanding of stellar evolution in different environments.

Despite these insights, the study has some limitations. The observational data were obtained using a 0.4m telescope, which may not have the resolution to detect fainter stars or resolve closely spaced stars. Additionally, the star finder function and the background noise estimator used in the data analysis may have introduced errors into the photometric measurements and the resulting HR diagrams. These functions assumed all the stars in the image to have the same size, which may not be accurate and could contribute to the errors.

Given these limitations, future research could benefit from the use of more powerful telescopes and more sophisticated data analysis methods. For example, adaptive optics could be used to improve the resolution of the images, and machine learning algorithms could be employed to enhance the accuracy of the star finder function and the background noise estimator. Furthermore, the assumptions about the size of the stars could be refined to improve the accuracy of the photometric measurements.

The findings from this study could also inform future research into specific aspects of stellar evolution. For instance, the data from M20 could be further analyzed to understand the nuances of stellar formation in nebulae, while the data from M7 could be used to explore the evolution of stars in open clusters.

References

[1] Wien's displacement law. http://hyperphysics.phy-astr.gsu.edu/hbase/wien.html. Accessed: 2023-05-28.

[2] Centre de Données astronomiques de Strasbourg. The simbad astronomical database. https://simbad.u-strasbg.fr/simbad/, 2023. Accessed: 2023-05-28.

[3] L. Eyer and N. Mowlavi. Variable stars across the observational hr diagram. 2007.

[4] R. M. Humphreys. The complex upper hr diagram. 2020.

[5] D. Kurtz. Asteroseismology across the hr diagram. 2022.

[6] M. J. P. F. G. Monteiro. Asteroseismology across the hr diagram. 2007.

[7] NASA. Messier 20: The trifid nebula, 2017. [Online; accessed 28-May-2023].

[8] Las Cumbres Observatory. Visibility tool, 2023. Accessed: 2023-05-28.

[9] I. Ramirez, C. Allende Prieto, D. L. Lambert, L. Koesterke, and M. Asplund. Granulation across the hr diagram. 2009.

[10] Wikipedia contributors. Hertzsprung–russell diagram — Wikipedia, the free encyclopedia, 2023. [Online; accessed 28-May-2023].

[11] Wikipedia contributors. Messier 7 — Wikipedia, the free encyclopedia, 2023. [Online; accessed 28-May-2023].